



ORIGINAL RESEARCH ARTICLE

# Characterization of (AlCrTiVZr)N High-Entropy Coating Produced by Cathodic Arc Evaporation

Alex Lothrop, Qi Yang, Xiao Huang, and Xiaohua Wu

Submitted: 2 February 2023 / Accepted: 23 May 2023 / Published online: 14 July 2023

**High-entropy alloy nitride (HEN) coating of (AlCrTiVZr)N was deposited onto 17-4PH stainless steel substrates using the cathodic arc evaporation (CAE) technique. The composition and resulting microstructure were analyzed, and key mechanical properties including solid particle erosion resistance and sliding wear resistance were measured in the as-deposited condition. The coating had a relatively rough surface and contained small spherical droplets and large splats throughout the coating thickness. It had a single-phased solid solution B1 nitride phase with a preferred (111) orientation. The coating retained the as-deposited microstructure upon high temperature annealing, but experienced nitride phase decomposition at a temperature 800 °C or above. The hardness of the as-deposited nitride fell into the range of  $27.5 \pm 2.10$  GPa and its elastic modulus was  $284 \pm 23$  GPa. Dry sliding wear tests revealed the higher wear rates of the coating when compared with the wear rates of TiN coatings under various testing conditions. The coating had an erosion rate that increased with the impingement angle and demonstrated a combination of ductile and brittle erosion damage modes. Comparing to the CAE deposited TiN coating, the HEN nitride coating showed a lower wear and erosion resistance, which is attributed to the presence of a large quantity of defects in the coating. Reducing number of droplets/splats becomes very important for having better high-entropy nitride coating quality and hence the better coating performance against wear and erosion.**

**Keywords** cathodic arc evaporation, erosion, high-entropy nitride coatings, thermal stability, wear

## 1. Introduction

High-entropy alloys (HEA) belong to a class of alloys that are composed of five or more principal elements, each making up 5 to 35 atomic percent (Ref 1). HEAs have many unique properties including high mixing entropy, sluggish diffusion, severe lattice distortion and the formation of stable single-phase solid solutions without formation of intermetallic compounds (Ref 2, 3). In recent years, there has been significant research undertaken on high-entropy nitride (HEN) coatings due to the desirable material characteristics including high hardness, strength, and fracture toughness, as well as high temperature oxidation, corrosion, and wear resistance (Ref 3-5).

Within the field of high-entropy nitride coatings, there is significant variation in findings due to a wide range of compositions, deposition methods and process parameters. Many studies focus on the effects of processing parameters, especially nitrogen ratio ( $R_N$ ) and substrate bias voltage, on the microstructure and mechanical properties of various HEA nitride coatings. In comparing studies with similar compositions, many studies such as those by Kuczyak on (AlCrTa-

TiZr)N, (AlCrMoTaTiZr)N, (AlCrNbSiTiV)N coatings with a single-phase FCC structure found an optimal hardness of 35.5 GPa, with increasing hardness attributed to grain refinement with increasing bias (Ref 6). A study by Cui et al. on (AlCrTiZrHf)N coatings found that at  $R_N = 0$ , the coatings have an amorphous structure, which transitions to a single solid solution FCC structure at increasing  $R_N$ , as the high-entropy effects inhibit the formation of intermetallic compounds resulting in a high coating hardness (33.1 GPa) and high wear resistance (Ref 7). Similar findings were made by Chang et al. revealing a (AlCrTaTiZr)N coating with an optimum hardness of 30 GPa (Ref 8). The above-mentioned coatings all have high hardness and many show promise as protective coatings.

These promising results encouraged further research into HEA nitride coatings. While the effects of processing parameters and nitrogen content on the microstructure and mechanical properties were extensively studied for various high-entropy nitride coatings, significantly less efforts have been made to reveal their performance as potential protective coatings against wear (Ref 9-11) and no research has been reported yet on the solid particle erosion performance of HEN coatings.

In terms of coating deposition technologies, most research works utilized magnetron sputtering, one of the physical vapor depositions (PVD) techniques, to deposit HEN coatings (Ref 7-11). Cathodic arc evaporation (CAE), as another widely used PVD deposition technique, which demonstrates several advantages over the magnetron sputtering, such as higher deposition rates, higher ionization ratio and better coating adhesion (Ref 6, 12). However, limited work has been done to produce HEN coatings using cathodic arc evaporation method (Ref 2, 5, 6). Therefore, it is one of the objectives of this study to explore

Alex Lothrop and Xiao Huang, Department of Mechanical and Aerospace Engineering, Carleton University, Ottawa, ON, Canada; and Qi Yang and Xiaohua Wu, National Research Council of Canada, Ottawa, ON, Canada. Contact e-mail: alexlothrop@cmail.carleton.ca.

CAE as a deposition technique for the high-entropy nitride coatings.

In this study, a target material of AlCrTiVZr was designed and used to deposit the high-entropy nitride (AlTiCrZrV)N coating by the CAE method in a reactive nitrogen atmosphere. Al and Ti were firstly chosen as the major elements as AlTiN coatings have demonstrated outstanding mechanical properties and tribological performance (Ref 13-15). Other alloying elements were selected, including Cr for oxidation and corrosion resistance due to its ability to form a stable surface oxide layer (Ref 16, 17), V for increased hardness and wear resistance (Ref 18, 19) and Zr for hardness and fracture properties improvement (Ref 20-22). The microstructure, thermal stability and mechanical properties of the coating were first characterized, and then dry sliding wear testing and solid particle erosion testing were performed to evaluate the coating performance pertinent to industrial applications.

## 2. Experimental

The (AlCrTiVZr)N coating was deposited using a Metaplas Ionon MZR-304 cathodic arc coater on polished 17-4 PH stainless steel flat disks of 50 mm in diameter and 3 mm in thickness. The following parameters were utilized based on some preliminary trials prior to this study. Two AlCrTiVZr cathodes, which consisted of 30%Al, 20%Cr, 20%Ti, 15%V and 15%Zr in atomic percentage were produced by hot-pressing and sintering. The cathodes were vertically mounted on two opposite walls of the coater. The flat disks were ultrasonically cleaned in alcohol and then loaded on a 2-axis of rotation carousel. Prior to coating deposition, the disks were ion cleaned with a bias of  $-280$  V using an arc enhanced glow discharge technique. During the deposition stage, a mixture of Ar and N<sub>2</sub> gases was introduced into the chamber with a fixed Ar flow rate of 150 sccm and regulated N<sub>2</sub> flow to achieve the constant pressure at 5 Pa (5E-2 mbar). A current of 85 A was employed on each cathode. A low bias voltage of  $-20$  V was applied on the carousel to provide ion bombardment and lower residual stress in the coating to avoid coating spallation. The deposition temperature was maintained at  $\sim 400$  °C and the total amount of ampere-hours (Ah) for coating deposition was 300 Ah, as the deposition time was 1 hour and 45 minutes. It should be noted the above processing parameters were optimized after several trial runs for better coating adhesion and low residual stress. The coated 17-4PH samples were used for microstructural and mechanical characterization as well as wear and erosion testing. For the transmission electron microscopic (TEM) analysis, silicon wafers were coated with the same coating composition, but at a shorter deposition time (25 min). The TiN coating was also deposited using the same CAE equipment with a similar deposition condition, but at a substrate bias of  $-100$  V, was characterized and evaluated as a baseline reference along with (AlCrTiVZr)N coating.

The surface and cross sections of the coating were examined using a Philips XL30 field emission scanning electron microscope (SEM) equipped with an energy-dispersive x-ray spectrometer (EDS). Droplet size was measured using ImageJ software setting threshold values to select the color of droplets from SEM images. Cross-sectional transmission electron microscope (TEM) samples were prepared following standard dimpling and ion milling procedures and examined in a JEOL

JEM 2100F operating at 200 kV. The surface roughness was measured by a Bruker DektakXT profilometer using an average of 6 measurements. The crystal structure of the coating was investigated using a Bruker AXS D8 Discover diffractometer operating in the Bragg-Brentano configuration and using the Cu K $\alpha$  radiation with a wavelength of 1.5406 Å at 40 kV and 40 mA and within  $2\theta$  angles of 30 to 85°. High temperature XRD analysis was performed using Bruker AXS D8 Discover diffractometer equipped with an Anton Paar HTK 1200N high temperature oven. The measurements were carried out within a  $2\theta$  angle range of 33-69° at room temperature, 600, 800, 900 and 1000 °C in sequence. The sample was heated in the argon filled chamber at a heating rate of 15 °C per minute and held at the measurement temperature for 20 minutes prior to each scan. The Vickers hardness and Young's modulus were measured on the coating cross section using a CSEM nanohardness tester with a Berkovitch indenter. The maximum applied load was 50 mN and the results were averaged over 7 measurements.

Prior to wear and erosion testing, samples were tumbled for 30 minutes with a SiO<sub>2</sub> medium to reduce coating surface roughness. Wear properties of the coating were evaluated by pin-on-disk testing, which was performed using a WC-6%Co ball of 5 mm in diameter as the counter body to generate a wear track of 8 mm in diameter on the coating, with applied normal loads of 2 N, 10 N, sliding speeds of 10 cm/s, 20 cm/s and a sliding distance of 1 km. The frictional force, which was used to calculate the coefficient of friction, was recorded throughout the test. The depth profile of the wear track was measured along the radial directions using a surface profilometer at six locations, from which the average wear track area ( $A$ ) can be calculated and used to calculate the wear volume. The specific wear rate of the coating was obtained by normalizing its wear volume with the total sliding distance and the applied normal load.

The wear volume of the WC-6%Co ball was calculated according to Eq 1, from which the specific wear rate was calculated, where  $R$  was the ball radius  $r$  was the radius of the wear scar and  $h$  was the height of the worn surface (Ref 23).

$$h = R - \sqrt{R^2 - r^2} \quad (\text{Eq 1a})$$

$$\text{Wear Volume} = \frac{1}{3}\pi h^2(3R - h) \quad (\text{Eq 1b})$$

Erosion data was obtained at room temperature using an S.S. White Abrasive Jet unit (model HME) placed on a Sartorius balance ( $\pm 0.5$  g) to measure the erodent consumption. The particle dry air stream was directed toward the testing coupon through a silicon carbide nozzle with an inner diameter of 1.14 mm, as schematically shown in Fig. 1(a), at impingement angles from 30 to 90° in 15° increments. During testing, the coupon surface to nozzle tip distance (NTD) was set at  $38 \pm 1$  mm. The erodent used for the tests was sharp edged AccuBRADE-50 Blend #3 alumina (Al<sub>2</sub>O<sub>3</sub>), as shown in Fig. 1(b), with an average particle size of 50  $\mu\text{m}$ . The pressure of the dry air was set to 15.5 psi, resulting in an average particle velocity of 84 m/s (300 km/h). The particle feed rate was set to approximately 1 g/min. The sample weight loss due to erosion was measured using a precision balance with an accuracy of  $10^{-5}$  g and used to calculate the erosion rate. The erosion rate was calculated from the slope of the line of the best fit for the sample weight loss versus erosion medium consumption curve obtained for each tested angle. Sample weight and erodent

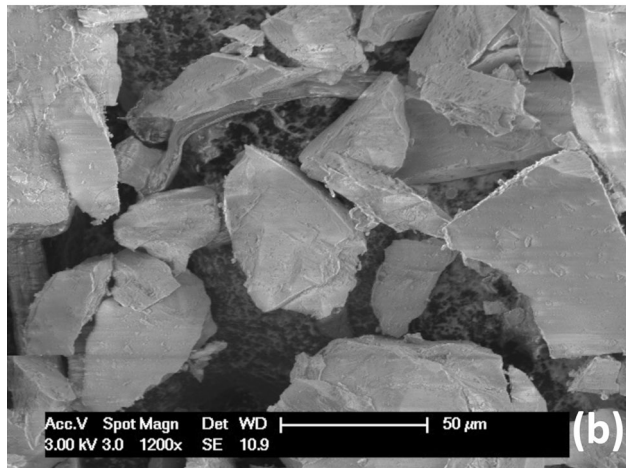
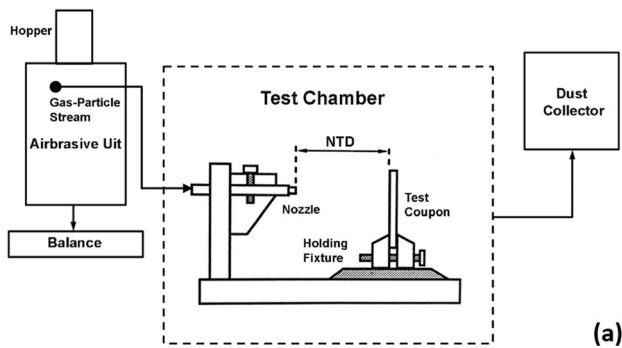


**Fig. 1** (a) Schematics showing the erosion testing setup and (b) the  $\text{Al}_2\text{O}_3$  erosion medium used for erosion testing

consumption measurements were recorded at three or more points throughout the test. Erosion tests were terminated once the substrate started to be exposed at the center of the erosion scar.

### 3. Results and Discussion

#### 3.1 Microstructural Characterization

Figure 2 shows the surface morphologies of the as-deposited (AlCrTiVZr)N and TiN coatings. While the TiN coating surface is smooth with few visible droplets (Fig. 2c), the (AlCrTiVZr)N coating has a much rougher surface (Fig. 2a). Splats, as shown in Fig. 2(b), are also observed on the (AlCrTiVZr)N coating surface, indicating the occurrence of solidifying impacted molten particles during the deposition process. (AlCrTiVZr)N coatings have a surface roughness of  $1.41 \pm 0.07 \mu\text{m}$ , significantly higher than that of TiN coating ( $0.402 \pm 0.08 \mu\text{m}$ ). Cross-sectional SEM images of the (AlCrTiVZr)N coating and the TiN coating are presented in Fig. 3. From the cross section, the average coating thickness of the (AlCrTiVZr)N coating was measured as  $25.2 \pm 0.22 \mu\text{m}$ . In the coating layer itself, a significant number of “defective” particles are seen in the nitride matrix. There are two different types of particles with different shapes, sizes, and chemical compositions. Some of them are small and spherical with a diameter usually less than  $2 \mu\text{m}$ , which is typical of droplets in coatings deposited using CAE, such as in the TiN coating as shown Fig. 3(c). Other particles are splats that have irregular shapes and the size much

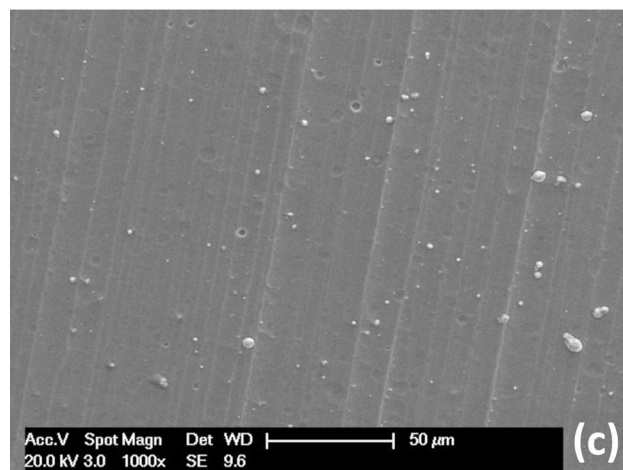
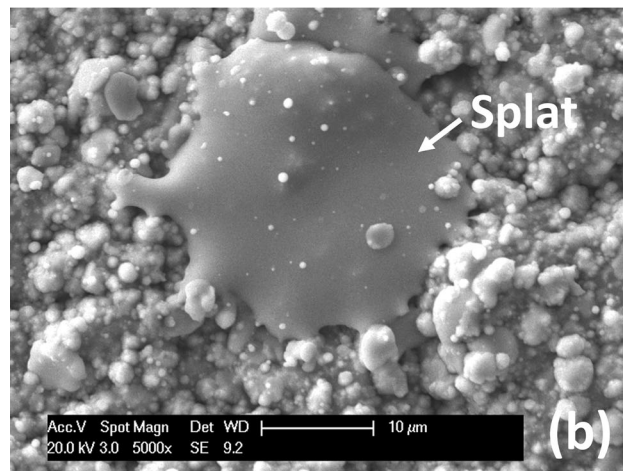
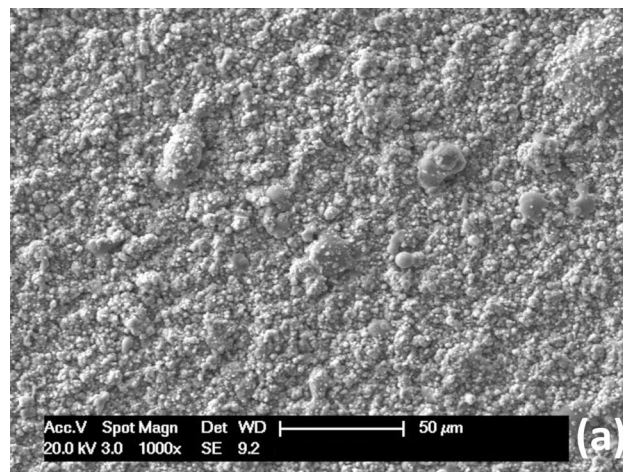


**Fig. 2** SEM images of as-deposited (AlCrTiVZr)N coating surface (a) (b) and as-deposited TiN surface (c)

larger than that of the spherical droplets. The spherical droplets and splats make up 7.8% of the coating cross-sectional area, significantly higher than that in the TiN coating where only few small spherical droplets can be observed. SEM analysis acquired under the backscattered electron (BSE) mode clearly demonstrated the compositional difference among the nitride matrix and these two types of particles: dark matrix, gray splats, and white spherical droplets, as shown in Fig. 3(b).

EDS analyses were performed on the nitride matrix. The average compositions from small droplets and large splats



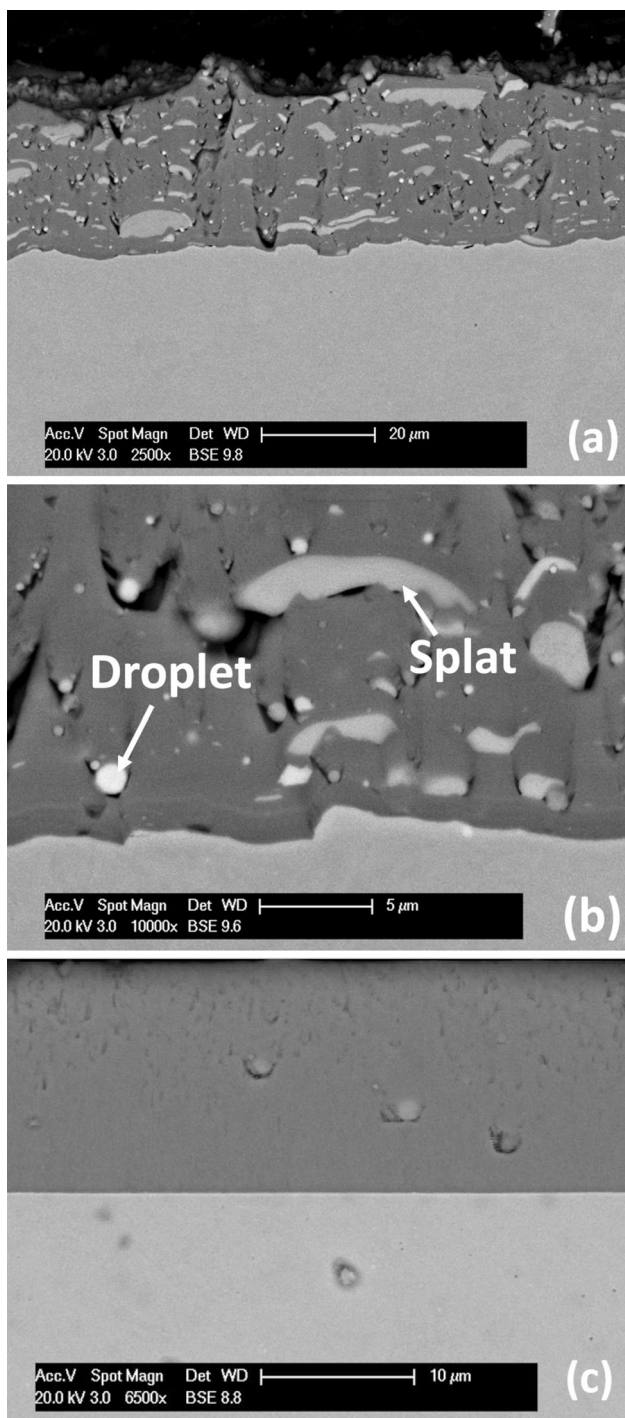


**Fig. 3** Cross-sectional image BSE SEM of (AlCrTiVZr)N (a), (b) and TiN (c) coating with splats and droplets indicated

acquired from four measurements at different locations are listed in Table 1. The metallic constituents in the nitride phase are found to have atomic ratios different from the cathode material, with a significantly higher ratio of aluminum, as reported for other multicomponent nitride coatings produced by CAE (Ref 24). Similarly, other work has reported a deficit of heavier elements in the nitride, including Zr when depositing HEA coatings by CAE (Ref 6). The splats contain 40 at.% nitrogen, less than that in the nitride matrix (50 at.% nitrogen). This observation suggests that these splats partially reacted with nitrogen. Moreover, the spherical droplets, different from the splats, were free of nitrogen.

Spherical droplets and splats are believed to originate from the molten particles ejected and splats from cathode arc spots. Small liquid particles are cooled faster, as well as fly faster, than larger ones, so they can reach to the sample surface in a spherical solid form (Ref 25, 26). It is suggested that these smaller droplets form a nitride shell which solidifies during flight across the chamber, and the interior of the droplet is unreacted (Ref 27). Large slow flying ejected liquid particles instead take longer time to reach the substrate, allowing sufficient time to partially react with nitrogen ions while remaining in the liquid state when they impact the sample surface. These large liquid particles were flattened and then solidified to form irregularly shaped splats. As the nature of the cathode material strongly affects the size and the amount of ejected liquid particles, the cathodes consisting of elements with higher melting points form fewer and smaller molten particles (Ref 25). The formation of many large splats in the (AlCrTiVZr)N coating indicates a relatively low melting point of the AlCrTiVZr type cathode material.

The XRD spectrum of the (AlCrTiVZr)N HEN coating (Fig. 4) shows that the coating has primarily a single solid solution nitride phase assuming a NaCl type B1 FCC structure. The (111) diffraction peak is very strong indicating the preferential crystal orientation. Accompanying the (111) peak, are weaker peaks corresponding to the (200) and (220) planes. The formation of the single solid solution nitride phase is attributed to the increased solid solubility and reduced long-distance diffusion of HEAs (Ref 28). In addition to peaks from the nitride phase, the presence of other peaks particularly in the 38–46° range indicates that a hexagonal close packed (HCP) metallic phase and possibly intermetallic compounds present in the droplets and splats. Based on the Scherrer's equation (Ref 29), the average nitride crystallite size of 25 nm is calculated. Furthermore, the nitride phase has a calculated lattice parameter,  $a$  of 4.14 Å. The TiN coating has the same B1 structure, with the strongest (111) peak at  $2\theta = 36.6^\circ$  corresponding similarly to the preferred (111) orientation.

Figure 5 presents the cross-sectional bright-field TEM images of the (AlCrTiVZr)N HEA nitride coating. From Fig. 5(a), the columnar coating growth and the presence of droplets in the coating in the form of spherical particles and the

**Table 1** (AlCrTiVZr)N coating matrix, splat, and droplet compositions, at.%

	Al	Cr	Ti	V	Zr	N
Nitride matrix	27.0 ± 0.7	8.7 ± 0.2	6.8 ± 0.1	4.9 ± 0.3	2.7 ± 0.1	50.0 ± 1.3
Splat	16.0 ± 0.3	7.0 ± 0.3	20.6 ± 0.5	9.8 ± 1.4	7.3 ± 0.3	39.3 ± 2.1
Droplet	26.5 ± 1.5	9.2 ± 0.7	29.7 ± 2.3	19.1 ± 2.2	15.6 ± 3.0	0

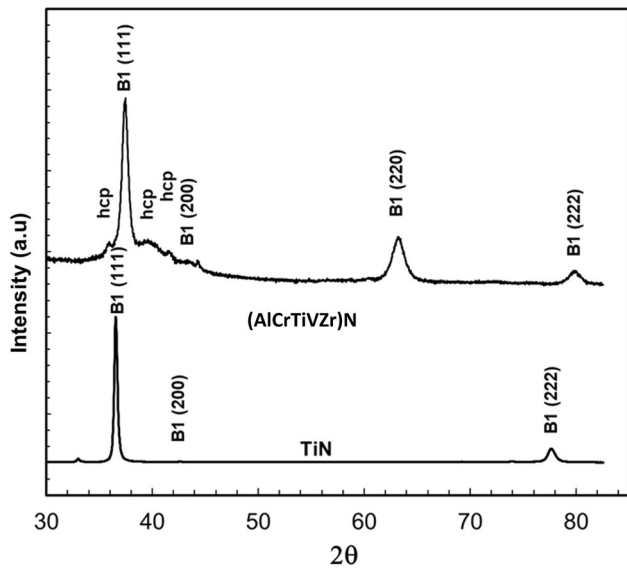


**Fig. 4** XRD spectra of (AlCrTiVZr)N and TiN coatings

associated porosity around it is clearly observed. A layered structure seen in the TEM image is resulted from the alternate exposure of the substrates placed on the rotating fixture to the two cathodes during deposition. The nitride matrix has a uniform texture, and no secondary phases are observed, i.e., it assumes a single solid solution nitride phase. The selected area electron diffraction pattern in Fig. 5(a) reveals diffraction rings for (111), (200), (220) and (222) crystal planes, confirming that the nitride matrix has an FCC B1 structure. The high-resolution TEM image in Fig. 5(b) clearly shows the (111) crystallographic planes with the interplanar distance of approximately 0.236 nm.

### 3.2 Mechanical Properties

The (AlCrTiVZr)N high-entropy nitride matrix has a hardness of  $27.5 \pm 2.1$  GPa, comparable to the hardness of the TiN coating at  $26.6 \pm 0.7$  GPa, but its elastic modulus of  $284 \pm 23$  GPa is significantly lower than that of TiN,  $417 \pm 5$  GPa. The measured hardness of the large splats in (AlCrTiVZr)N HEA coating varied in a range of 13.5–18 GPa with an average of  $15.9 \pm 2.0$  GPa, markedly lower than that of the nitride matrix due to the lower nitrogen content. The hardness and elastic modulus of the spherical droplets could not be measured due to their small size. However, because of their metallic nature, they are expected to be much softer than the nitride matrix. The presence of a large quantity of droplets and splats in the coating, therefore, lowers the bulk hardness of the coating, consequently affecting the coating's performance.

### 3.3 Thermal Stability

To investigate the thermal phase stability of the (AlCrTiVZr)N coating, the XRD spectra were also obtained after holding the coating for 20 minutes at 600, 800, 900 and 1000 °C. As shown in Fig. 6, no obvious change could be detected when the temperature increased from room temperature to 600 °C. When the temperature further increased to 800 °C, a broad hump, as marked by a circle, started to appear in the  $2\theta$  angle range between 40 and 45° while the B1 (111) and B1 (220) nitride peaks remained unchanged. The broad

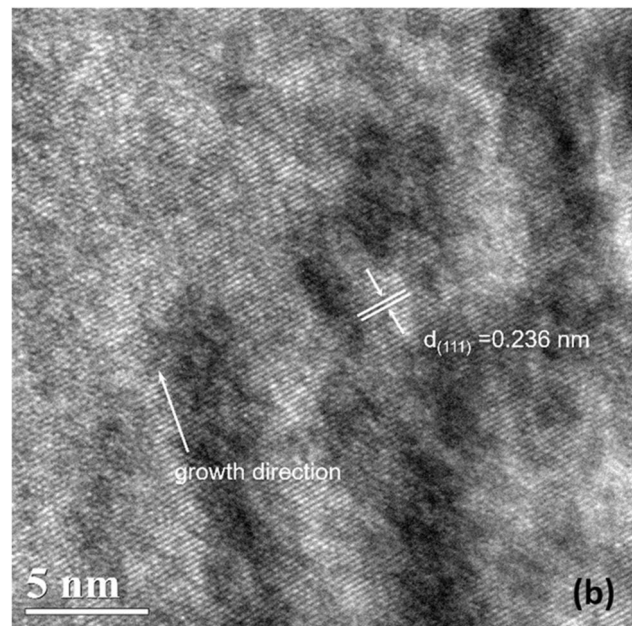
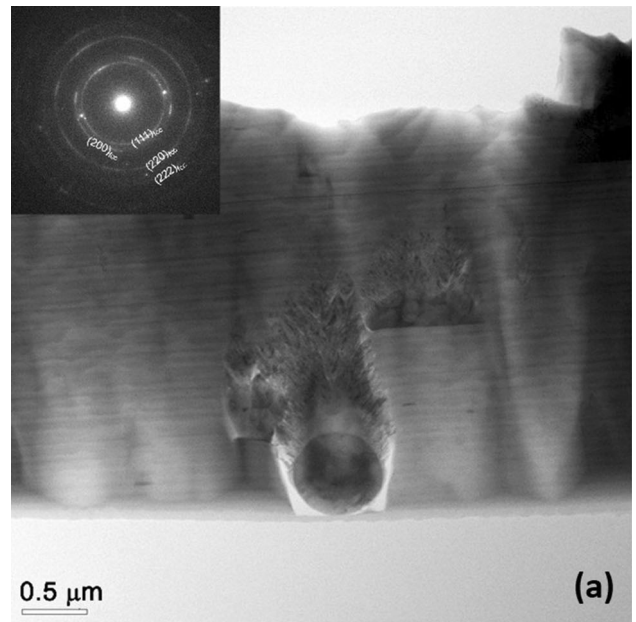


**Fig. 5** Cross-sectional TEM images of the (AlCrTiVZr)N high-entropy nitride coating: (a) low magnification image with the insert showing selected area electron diffraction pattern from the coating layer and (b) high-resolution TEM lattice image

hump indicates that at temperatures higher than 800 °C, the HEA nitride (AlCrTiVZr)N coating experienced decomposition from a primarily single solid solution nitride phase to multiple nitride phases. The peak positions of the (111) and (200) orientation of ZrN, TiN, CrN and VN are indicated in Fig. 6. The overlap of these (200) peaks appears to form the broad hump in the 40 and 45° range. After further increasing the temperature to 900 °C, the B1 (111) and B1 (222) (AlCrTiVZr)N nitride peaks showed a clear shift in their positions. For instance, the (111) peak remained at  $2\theta$  angle of approximately 37.59° from room temperature to up to 800 °C but shifted to 37.71 and 37.92° at 900 and 1000 °C, respectively. This can be translated to the lattice parameter value 4.140 Å in the 25–800 °C range, but a reduction to

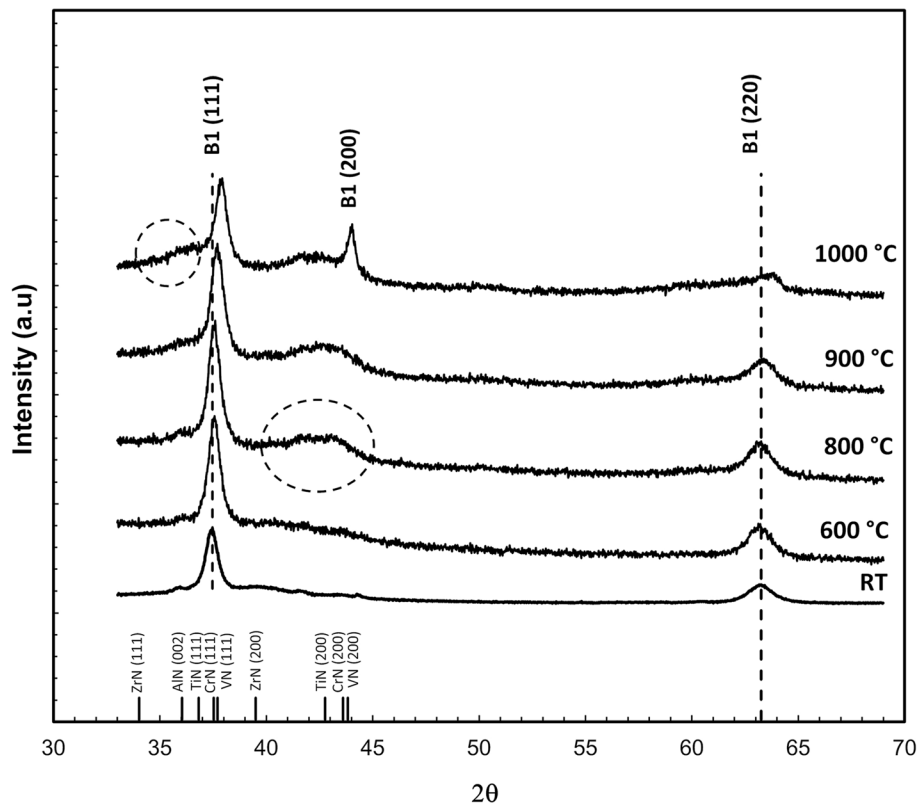


**Fig. 6** High temperature XRD of (AlCrTiVZr)N coatings

4.127 Å at 900 and 4.105 Å at 1000 °C. The decrease in the lattice parameter is attributed to the release of compressive stress in the coating (Ref 30, 31). At 1000 °C, in addition to the broad hump in the  $2\theta$  angle range of  $\sim 34\text{--}37^\circ$ , observed also at 800 and 900 °C, related to the partially decomposition of the high-entropy solid solution nitride phase to FCC structured CrN, TiN, VN, ZrN and hexagonal AlN. Additionally, the appearance of a distinct and strong B1 (200) peak has been detected, indicating the start of the recrystallization of the high-entropy nitride phase. A similar decomposition of a high-entropy nitride has been reported for (AlTiVNbCr)N (Ref 32) and (HfTaTiVZr)N (Ref 33).

### 3.4 Coating Performance

The wear resistance of the coatings was evaluated for a variety of wear conditions through dry sliding against WC-Co ball. The coefficient of friction (COF) of the (AlCrTiVZr)N coating after wear testing at the maximum load and speed (20 cm/s, 10N), is shown in Fig. 7, where it peaked rapidly during the running in stage, then quickly declined and reached a steady state value of 0.54 for the remaining duration of the test. In contrast, after the initial fast increase, the coefficient of friction of TiN increased slowly and then maintained a steady state value of 0.45 after sliding more than 200 m. Similar profiles were noted for the other wear conditions. At the lower speed of 10 cm/s, the COF increased (0.66 for (AlCrTiVZr), 0.56 for TiN) and at the reduced load of 2N, the friction force was decreased but the COF which is normalized against load increased (0.8 for (AlCrTiVZr), 0.75 for TiN).

In comparing the wear tracks from the 20 cm/s, 10N wear test, after sliding for 1 km the wear track on the (AlCrTiVZr)N

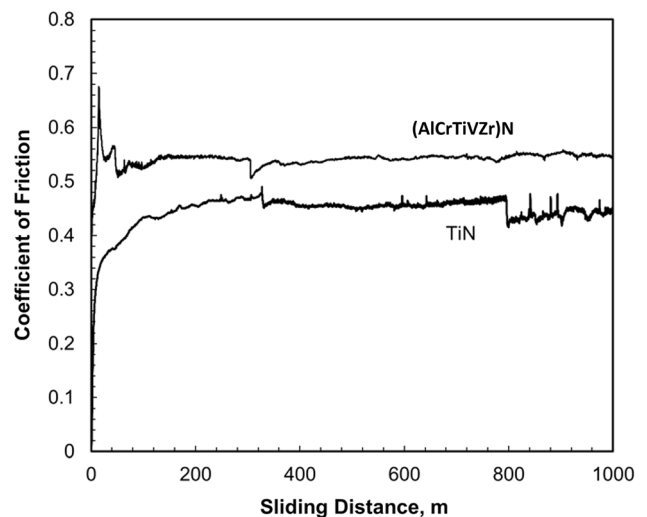


**Fig. 7** Coefficient of friction vs. sliding distance plots of (AlCrTiVZr)N and TiN coatings

coating had an average width of 0.67 mm and an average maximum depth of 14.8  $\mu\text{m}$ . The wear track of TiN, on the other hand, was narrower; with a width of 0.48 mm and shallower with a maximum depth of 3.4  $\mu\text{m}$ . The wear volume increased with decreasing speed and increased load, and similar observations between the (AlCrTiVZr)N and TiN coatings were made for the other wear conditions. Figure 8 shows the specific wear rates of the (AlCrTiVZr)N and TiN for varying conditions. The wear rates of the (AlCrTiVZr)N coating vary between  $7.2\text{E-}6$  and  $1.5\text{E-}5$   $\text{mm}^3/(\text{m}\cdot\text{N})$ . For both coatings, the



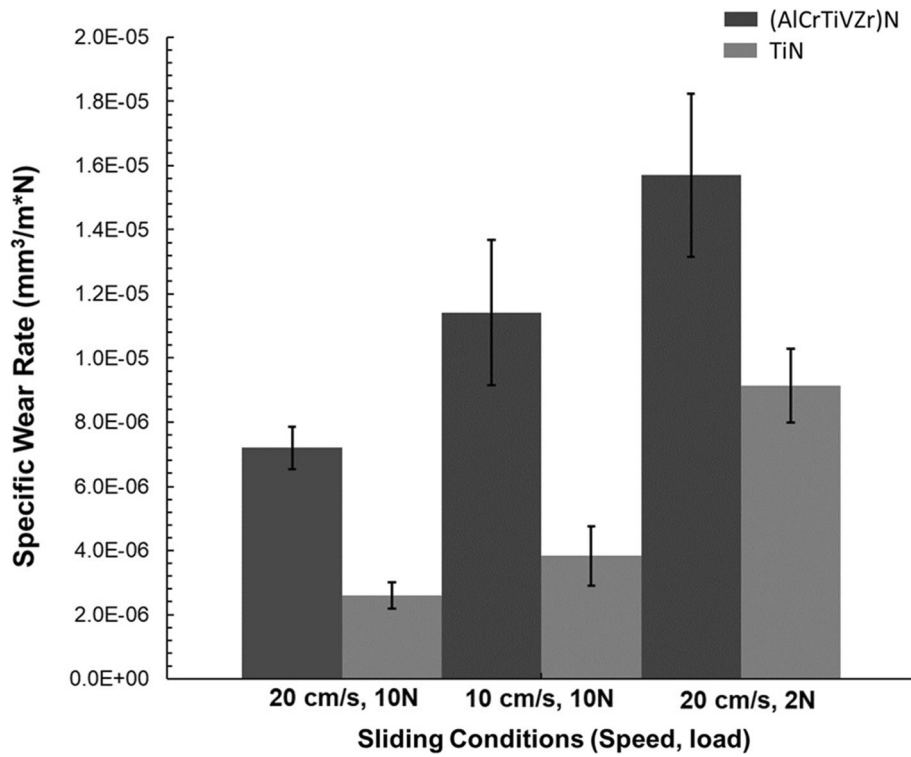


Fig. 8 Specific wear rates of (AlCrTiVZr)N and TiN coatings at varying wear conditions

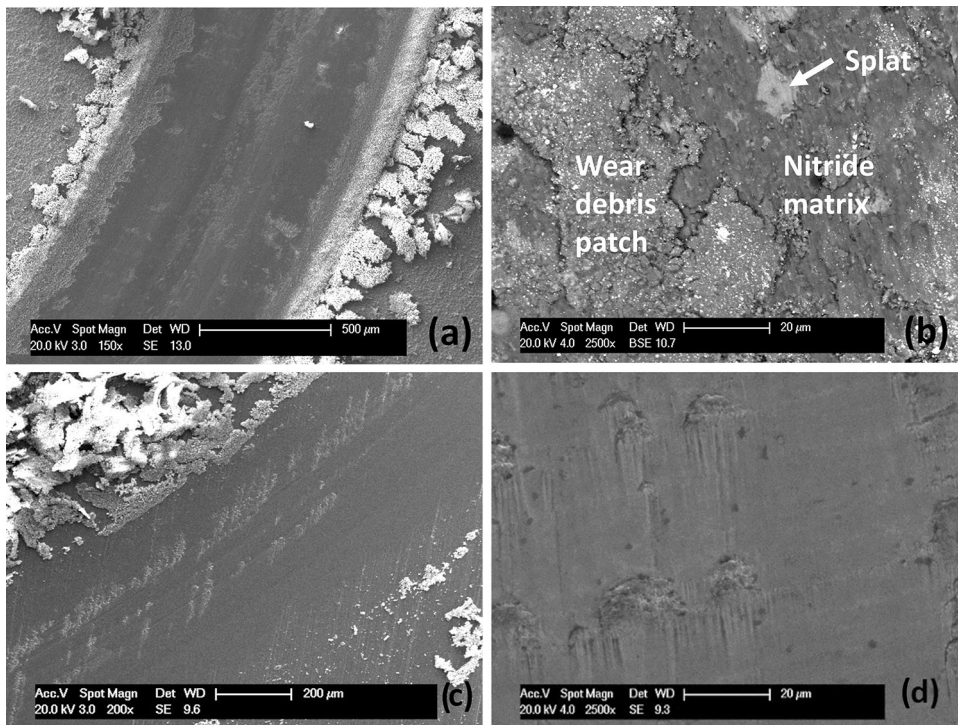


Fig. 9 SEM images of wear tracks of (AlCrTiVZr)N coating (a), (b), and TiN coating (c), (d)

wear rate increases for the 10 cm/s, 10 N load condition. For the 20 cm/s, 2N load condition, the wear rate increases as the wear volume does not vary proportionally with load. The wear rates of the (AlCrTiVZr)N coating is consistently higher by 1.7-

3.0 times than those of TiN coating but 1/60th that of the wear rate of the uncoated 17-4PH substrate ( $4.14E-4 \text{ mm}^3/(\text{m}\cdot\text{N})$ ), highlighting the benefits of applying protective coatings.

**Table 2** (AlCrTiVZr)N wear track compositions, at.%

	Al	Cr	Ti	V	Zr	N	O	Co	W
Wear debris	17.0	5.7	5.7	4.1	2.3	35.1	20.9	0.7	2.6
Nitride matrix	26.9	8.4	7.1	5.1	3.3	49.3	0	0	0
Splat	19.7	8.6	18.1	11.6	6.9	35.1	0	0	0

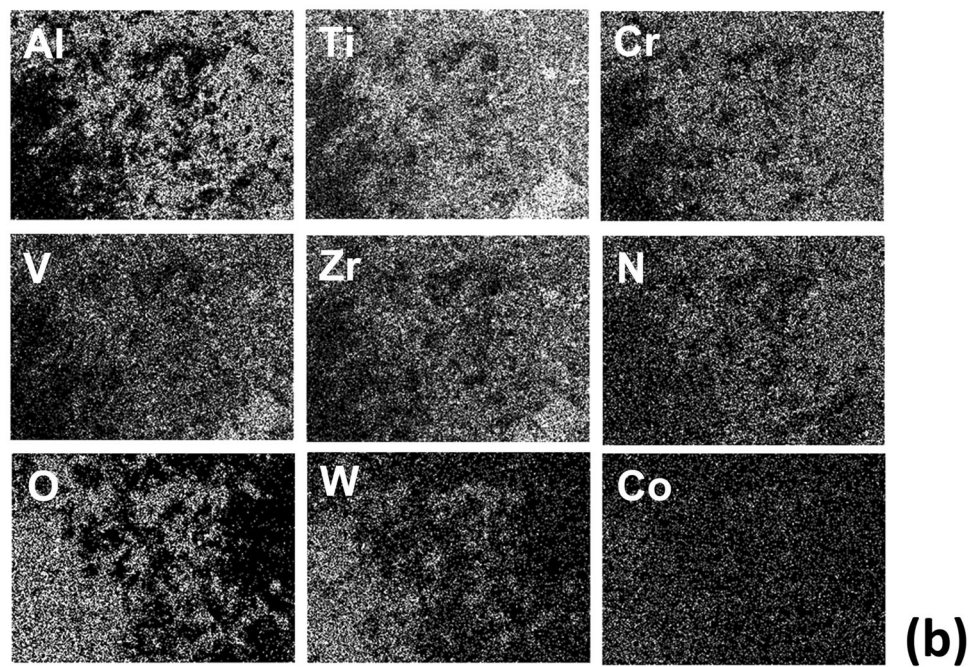
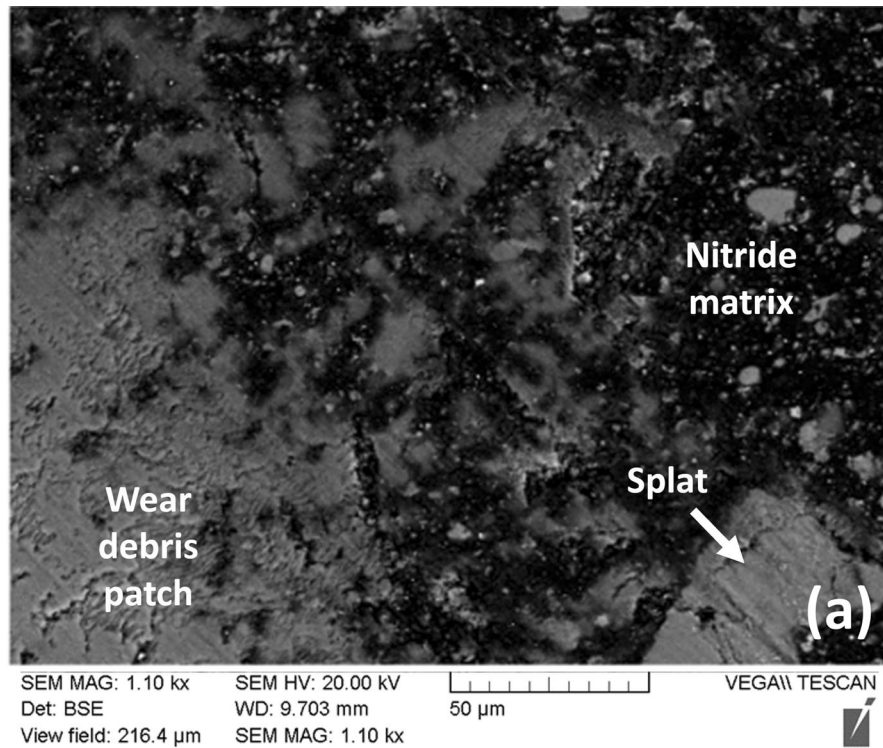


**Fig. 10** (a) BSE image and (b) EDS map of (AlCrTiVZr)N wear track after wear test (10N, 10 cm/s)



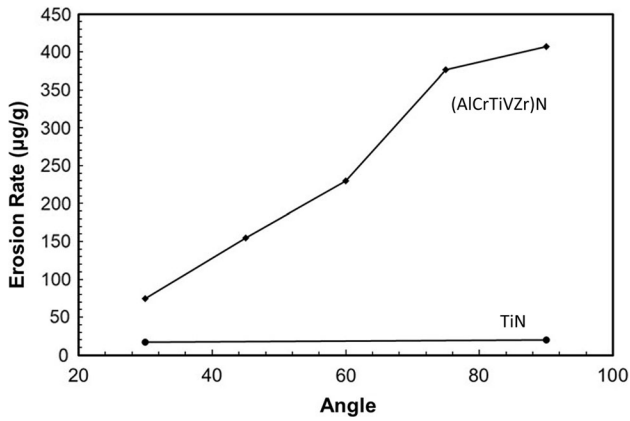


**Fig. 11** Erosion rate of (AlCrTiVZr)N coating and TiN coating at 30-90°

The SEM images showing the wear tracks of the (AlCrTiVZr)N coating and TiN after sliding conditions of 20 cm/s, 10N are presented in Fig. 9. Wear debris can be observed to accumulate near the edge of the wear tracks (Fig. 9a and c). EDS analysis of this wear debris from the (AlCrTiVZr)N coating surface reveals that is primarily composed of the elements of the nitride matrix with the same relative concentrations. The wear debris has a lower concentration of nitrogen (~35 at.%) as the debris has been partially oxidized (~20 at.%). It also contains trace amounts of transferred material from the WC-Co ball. As the debris still contains a significant amount of N, the displaced coating materials is believed to have been only partially oxidized during dry sliding process, reflecting the relatively fast coating material removal. The wear track surface is rough and is composed of three regions of distinct compositional differences, as shown in Fig. 9(b) with the compositional analysis provided in Table 2. The first is regions of smeared wear debris, with a similar composition to the debris surrounding the wear track. Additionally, regions of exposed nitride are visible, with no oxygen or ball debris. Finally, due to their large sizes, splats

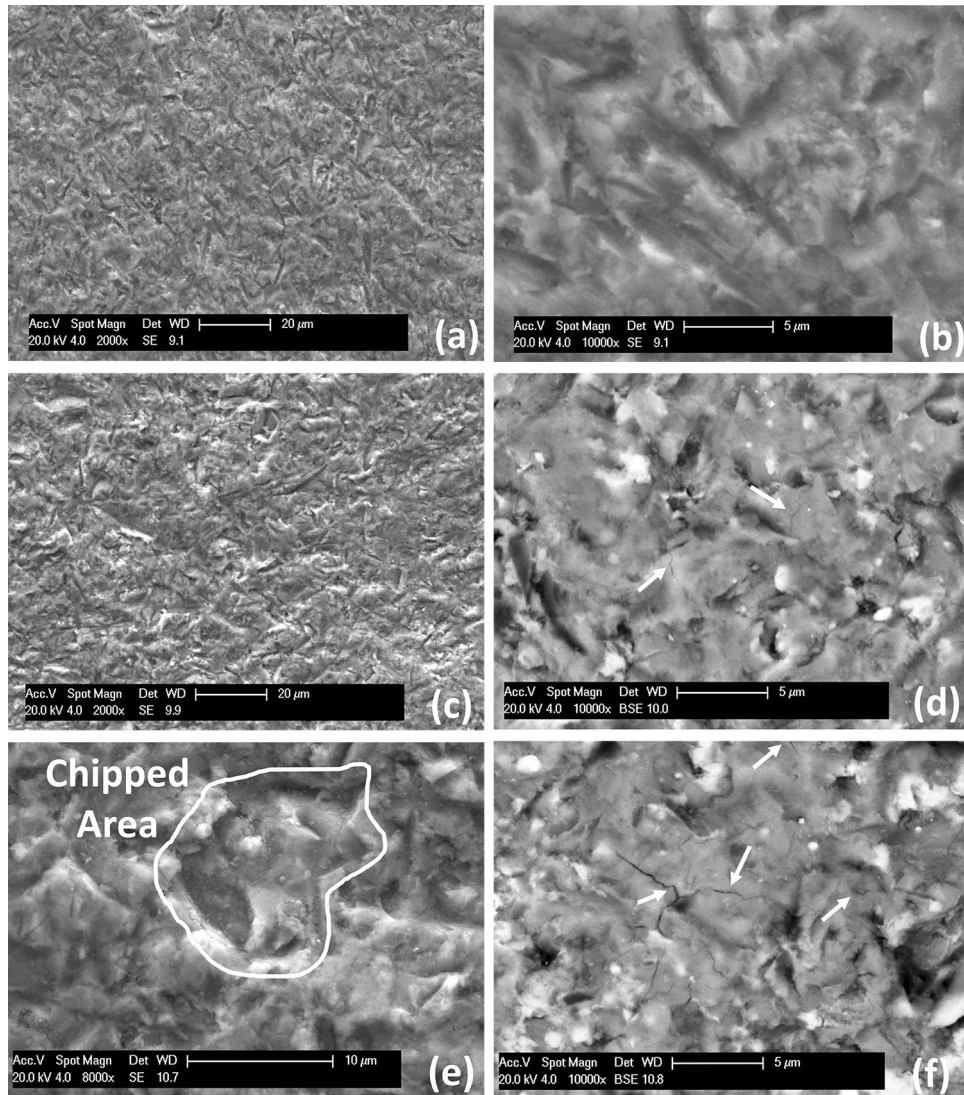


**Fig. 12** SEM images of erosion scar for the test: at 30° showing long cutting marks (a), (b), at 60° showing cutting marks (c) and some shallow cracks as indicated by arrows in (d), and 90° showing short cutting marks and chipping (e) with larger cracks (f)

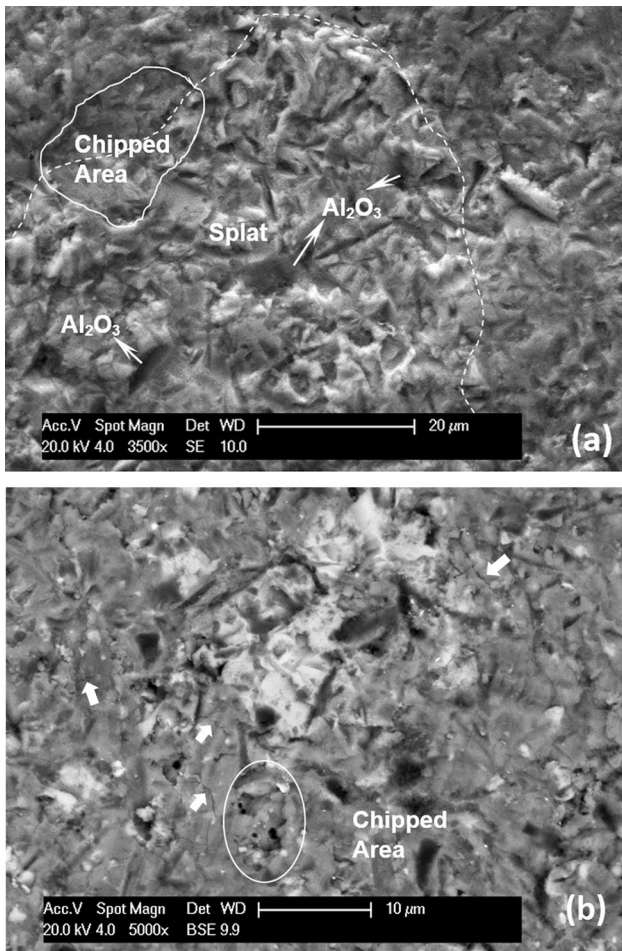


**Fig. 13** SEM images showing deep cutting marks within dash line enclosed splat (a). Coating adjacent to splats are prone to chipping (the chipped areas are indicated by solid lines in (a) and (b)) and cracking as shown by the arrows in (b). The images were taken from the sample tested at 60°

can be seen on the wear track surface. The splat retains it as deposited composition and has not oxidized during sliding. An EDS map of the wear track showing the regions of compositional difference is included in Fig. 10. In comparison, the TiN coating wear track surface is smoother and covered with less wear debris patches (Fig. 9d).

The nitride phase in the (AlCrTiVZr)N coating had a higher hardness and lower elastic modulus, hence a higher  $H^3/E^2$  ratio and a higher resistance to plastic deformation compared to those of the TiN coating. However, the (AlCrTiVZr)N coating demonstrated lower wear resistance than TiN. The reasons are as follows: a relatively large number of soft splats and droplets

in the coating significantly reduced the overall coating hardness; these coating defects were easily to be worn out not only because they were soft, but also because they were surrounded by voids. Secondly, the partially oxidized wear debris on the wear track in turn served as an abrasive increasing the wear. The higher friction force of the (AlCrTiVZr)N coating is another factor for its higher wear rate than that of TiN.

Figure 11 shows mass erosion rates at various angles for the (AlCrTiVZr)N coating and TiN coating. For both coatings the erosion rates increased with impact angle. The erosion rate of (AlCrTiVZr)N coating increased from 74 μg/g at 30 to 407 μg/g at 90°. In comparison, the TiN had an erosion rate of 16.9 μg/g at 30 and 19.8 μg/g at 90°. Again, the difference in erosion rates can be attributed to the significant amount of the droplets and splats in the (AlCrTiVZr)N coating.

SEM images of the erosion scars of the (AlCrTiVZr)N coating are presented in Fig. 12. At all angles, cutting marks left by impinging particles are visible and their length becomes shorter as the impinging angle increases. At 60°, some cracks as indicated by the arrows in Fig. 12(d) appear in the vicinity of the cutting marks. At 90°, cracks appear more regularly, increasing in size and depth. Localized coating chipping is also observed, as noted in Fig. 12e). For solid particle erosion, there are different damage modes causing material removal. Ductile erosion damage occurs by micro-cutting and plowing and a material with a high hardness exhibits high resistance to this type of erosion. In brittle materials and under impingement at higher angles, damage occurs from cracking and chipping (Ref 34) and an improved toughness is needed to reduce the brittle erosion damage (Ref 35) especially with high particle impingement angle and/or velocity. The SEM images in Fig. 12 clearly demonstrate that the erosion of the (AlCrTiVZr)N coating falls under a combination of ductile and brittle damage mechanisms.

SEM analysis performed on the erosion damages of the droplets, splats and the surrounding nitride matrix indicated that the splats/droplets suffered more erosion damage, with deeper cutting marks resulting in rougher surface than the nitride matrix (Fig. 13a). Alumina particles are also observed to be embedded in the soft splats/droplets. Furthermore, the nitride adjacent to splats was believed to have been weakened and was prone to cracking and chipping (Fig. 13b) due to the significant difference in mechanical properties between them and the existence of gap/porosity between the nitride matrix and the splats. As the CAE process might produce a significant number of large splats in the high-entropy nitride coatings, as revealed in this study, the presence of these defective splats resulted in inhomogeneity in the coating microstructure and hence variation in their properties.

In addition to the large splats, the smaller droplets are also detrimental to coating's performance. A previous study on CAE of TiN coatings found that coating areas with more droplet defects had a lower cavitation erosion resistance than the areas

**Table 3** Wear rates of existing works on HEN coatings

Composition	Deposition technique	Hardness, GPa	Wear rate, E-6 mm <sup>3</sup> /N m	COF	Ref
(AlCrTaTiZr)N	Radio frequency magnetron sputtering	28.5-36.9	3.7-6.5	0.73-0.78	(Ref 38)
(AlCrMoTaTiZr)N	Radio frequency magnetron sputtering	24.1-40.2	2.8-2.9	0.74-0.80	(Ref 39)
(TiZrNbTaFe)N	High power impulse magnetron sputtering	21.6-36.2	1.0-3.7	0.69-0.79	(Ref 40)
(AlCrMoSiTi)N	Filtered cathodic arc evaporation	19.5-41.6	3.2-5.4	0.51-0.55	(Ref 5)



with less or no droplets (Ref 36). Droplets also negatively influenced the wear resistance of TiAlTaN coatings by introducing cracks and fragments which acted as abrasive medium in the wear debris (Ref 37). Droplets were found to be responsible for the extremely rough surface of the (AlCrTiV)N coatings deposited by CAE (Ref 30), same as that found in this research.

Overall, the (AlCrTiVZr)N coating produced by CAE did not perform as well as the conventional TiN coating in terms of wear and erosion resistance. The existing studies reporting on the wear rates of various HEN coatings, such as magnetron sputtering deposited (AlCrTaTiZr)N (Ref 38), (AlCrMoTaTiZr) (Ref 39), (TiZrNbTaFe)N (Ref 40) and filtered cathodic arc evaporated (AlCrMoSiTi)N (Ref 5), which are in the range of  $1.0\text{E-}6$  -  $6.5\text{E-}6$   $\text{mm}^3/(\text{m}\cdot\text{N})$  as presented in Table 3. Clearly, they have lower wear rates than those of the (AlCrTiVZr)N coating ( $7.2\text{E-}6$  -  $1.5\text{E-}5$   $\text{mm}^3/(\text{m}\cdot\text{N})$ ) presented in this study. The existing studies reported COFs in a similar range from 0.5 to 0.9 and consistent observations of the wear track including a smooth curved surface and moderate oxidation of accumulated wear debris. The increased wear resistance of these coatings can be explained by their different hardness and most importantly the lack of coating defects, such as droplets or especially the large size splats.

Unlike the magnetron sputtering method which can produce high quality coatings with minimal number of coating defects due to the nature of the magnetron sputtering process, droplets are the common coating defects for the cathodic arc deposited coatings. When TiN, CrN and TiAlN coatings were deposited, the droplets in the coating are usually small in size and limited with numbers. Those coatings are good enough for many industrial applications. However, existing literature has identified droplet formation as a limitation of the CAE deposition method for HEN coatings (Ref 41, 42), like the finding in this study. Though ternary nitrides of AlTiN (Ref 43) and AlCrN (Ref 44) have been successfully deposited by CAE with limited amounts of droplets, additional factors may influence the melting of HEA targets. For example, it has been reported the adding Zr into CrNiFeCoMn high-entropy alloy leads to the formation of a eutectic with a low melting point (Ref 20). Lowering the melting temperature of the targets facilitates the formation of droplets. Clearly, there is a need to significantly reduce the number of large splats and the droplets to avoid their detrimental effects on coating surface roughness and performance. First, as the melting point of the HEA alloy cathode material has a strong effect on the generation of droplets and splats, a cathode material with a higher melting point should be selected when possible. Second, the macro-particle generation from the cathode(s) can be reduced through reducing the cathode temperature by employing effective cooling to the cathode(s) and accelerating the cathode spot motion (Ref 45). It becomes particularly important as the lattice distortion associated with HEAs increases phonon scattering, hence reducing the thermal conductivity and limiting the effect of target cooling (Ref 46, 47). Another approach is to separate the flux of molten droplets that are ejected from the cathode(s) by using electric or magnetic filtering so that they cannot be deposited as part of the coatings. This technique has led to the deposition of smooth and dense structured (AlCrMoSiTi)N (Ref 5) and AlCrNiTiV coatings (Ref 48) with reduced coating defects.

## 4. Conclusions

(AlCrTiVZr)N high-entropy nitride coating was deposited in this study by the CAE technique using parameters optimized from preliminary study. The resulting coating had a rough coating surface, large splats, and small spherical droplets throughout the coating thickness. XRD analysis revealed that the coating had a primary single-phased solid solution nitride phase with a preferred (111) crystallographic orientation parallel to the coating surface. The coating retained the as-deposited microstructure up to 800 °C, above which phase decomposition occurred. The as-deposited nitride had a hardness of  $27.5 \pm 2.10$  GPa and an elastic modulus of  $284 \pm 23$  GPa. Dry sliding wear tests determined higher wear rates for the (AlCrTiVZr)N coatings than those for TiN under various testing conditions. Sand particle erosion tests showed an increase in erosion rate with increasing impingement angles: an erosion rates of 74  $\mu\text{g/g}$  at 30 degrees and 407  $\mu\text{g/g}$  at 90 degrees. SEM images of the erosion scar revealed mixed erosion damage mode with cutting marks, coating cracking and chipping. The coating samples produced in this study had a lower erosion and wear resistance than a conventional TiN coating, suggesting that the large number of splats and droplet negatively impacted the coating performance. This work provided insight into droplets/splats formation and present possible approaches to reducing coating defects for future works if CAE would be used to produce high-entropy alloy nitride coatings.

## Acknowledgments

This study was conducted under the financial support from the New Ideation Program of the National Research Council of Canada (NRC) under project A1-019042. The authors would like to thank Kayvan Separi, Guy Parent and Andre Zborowski, all from NRC, for performing coating deposition, preparing the TEM sample, and performing the high temperature XRD analysis, respectively.

## Conflict of interest

The authors declare that they have no known competing financial interests or personal relationships that could have appeared to influence the work reported in this paper.

## References

1. J. Yeh, S. Chen, S. Lin, J. Gan, T. Chin, T. Shun, C. Tsau, and S. Chang, Nanostructured High-Entropy Alloys with Multiple Principal Elements: Novel Alloy Design Concepts and Outcomes, *Adv. Eng. Mater.*, 2004, **6**, p 299–303. <https://doi.org/10.1002/adem.200300567>
2. A. Pogrebnyak, V. Yakushchenko, A. Bagdasaryan, O. Bondar, R. Krause-Rehberg, G. Abadias, P. Chartier, K. Oyoshi, Y. Takeda, V. Beresnev, and O. Sobol, Microstructure, Physical and Chemical Properties of Nanostructured (Ti-Hf-Zr-V-Nb)N Coatings under Different Deposition Conditions, *Mater. Chem. Phys.*, 2014, **147**, p 1079–1091. <https://doi.org/10.1016/j.matchemphys.2014.06.062>
3. W. Li, P. Liu, and P. Liaw, Microstructures and Properties of High-Entropy Alloy Films and Coatings: A Review, *Mater. Res. Lett.*, 2018, **6**, p 199–229. <https://doi.org/10.1080/21663831.2018.1434248>
4. D. Moskovskikh, S. Vorotilo, V. Buinevich, A. Sedegov, K. Kuskov, A. Khort, C. Shuck, M. Zhukovskiy, and A. Mukasyan, Extremely Hard and Tough High Entropy Nitride Ceramics, *Sci. Rep.*, 2020, **10**, p 19874. <https://doi.org/10.1038/s41598-020-76945-y>

5. Y. Zhao, S. Chen, Y. Chen, S. Wu, W. Xie, W. Yan, S. Wang, B. Liao, and S. Zhang, Super-Hard and Anti-corrosion (AlCrMoSiTi)<sub>N<sub>x</sub></sub> High Entropy Nitride Coatings by Multi-arc Cathodic Vacuum Magnetic Filtration Deposition, *Vacuum*, 2022, **195**, p 110685. <https://doi.org/10.1016/j.vacuum.2021.110685>
6. M. Kuczyk, T. Krulle, M. Zawischa, J. Kaspar, O. Zimmer, M. Leonhardt, C. Leyens, and M. Zimmermann, Microstructure and Mechanical Properties of High Entropy Alloy Nitride Coatings Deposited Via Direct Current Cathodic Vacuum Arc Deposition, *Surf. Coat. Technol.*, 2022, **448**, p 128916. <https://doi.org/10.1016/j.surfcoat.2022.128916>
7. P. Cui, W. Li, P. Liu, K. Zhang, F. Ma, X. Chen, R. Feng, and P. Liaw, Effects of Nitrogen Content on Microstructures and Mechanical Properties of (AlCrTiZrHf)<sub>N</sub> High-Entropy Alloy Nitride Films, *J. Alloys Compd.*, 2020, **834**, p 155063. <https://doi.org/10.1016/j.jallcom.2020.155063>
8. S.Y. Chang, S.Y. Lin, Y.C. Huang, and C.L. Wu, Mechanical Properties, Deformation Behaviors and Interface Adhesion of (AlCr-TaTiZr)<sub>N<sub>x</sub></sub> Multi-component Coatings, *Surf. Coat. Technol.*, 2010, **204**, p 3307–3314. <https://doi.org/10.1016/j.surfcoat.2010.03.041>
9. Y.C. Lin, S.Y. Hsu, R.W. Song, W.L. Lo, Y.T. Lai, S.Y. Tsai, and J.G. Duh, Improving the Hardness of High Entropy Nitride (Cr<sub>0.35</sub>Al<sub>0.25</sub>Nb<sub>0.12</sub>Si<sub>0.08</sub>V<sub>0.20</sub>)<sub>N</sub> Coatings Via Tuning Substrate Temperature and Bias for Anti-wear Applications, *Surf. Coat. Technol.*, 2020, **403**, p 126417. <https://doi.org/10.1016/j.surfcoat.2020.126417>
10. C. Zhang, X. Lu, H. Zhou, Y. Wang, X. Sui, Z. Shi, and J. Hao, Construction of a Compact Nanocrystal Structure for (CrNbTiAlV)<sub>N<sub>x</sub></sub> High-Entropy Nitride Films to Improve the Tribo-Corrosion Performance, *Surf. Coat. Technol.*, 2022, **429**, p 127921. <https://doi.org/10.1016/j.surfcoat.2021.127921>
11. W. Lo, S. Hsu, Y. Lin, S. Tsai, Y. Lai, and J. Duh, Improvement of High Entropy Alloy Nitride Coatings (AlCrNbSiTiMo)<sub>N</sub> on Mechanical and High Temperature Tribological Properties by Tuning Substrate Bias, *Surf. Coat. Technol.*, 2020, **401**, p 126247. <https://doi.org/10.1016/j.surfcoat.2020.126247>
12. P. Martin, *Handbook of Deposition Technologies for Films and Coatings: Science, Applications and Technology*, Elsevier, Amsterdam, 2009
13. B. Beake, J. Endrino, C. Kimpton, G. Fox-Rabinovich, and S. Veldhuis, Elevated Temperature Repetitive Micro-scratch Testing of AlCrN, TiAlN and AlTiN PVD Coatings, *Int. J. Refract. Met. Hard Mater.*, 2017, **69**, p 215–226. <https://doi.org/10.1016/j.ijrmhm.2017.08.017>
14. J. Mo, M. Zhu, A. Leyland, and A. Matthews, Impact Wear and Abrasion Resistance of CrN, AlCrN and AlTiN PVD Coatings, *Surf. Coat. Technol.*, 2013, **215**, p 170–177. <https://doi.org/10.1016/j.surfcoat.2012.08.077>
15. W.D. Munz, Titanium Aluminum Nitride Films: A New Alternative to TiN Coatings, *J. Vac. Sci. Technol.*, 1986, **4**, p 2717–2725. <https://doi.org/10.1116/1.573713>
16. Y. Zhang, H. Wu, X. Yu, and Di. Tang, Role of Cr in the High-Temperature Oxidation Behavior of Cr<sub>x</sub>MnFeNi High-Entropy Alloys at 800 °C in Air, *Corros. Sci.*, 2022, **200**, p 110211. <https://doi.org/10.1016/j.corsci.2022.110211>
17. D.D. Xu, B.L. Zhou, Q.Q. Wang, J. Zhou, W.M. Yang, C.C. Yang, L. Xue, X.D. Fan, L.Q. Ma, and B.L. Shen, Effects of Cr Addition on Thermal Stability, Soft Magnetic Properties and Corrosion Resistance of FeSiB Amorphous Alloys, *Corros. Sci.*, 2018, **138**, p 20–27. <https://doi.org/10.1016/j.corsci.2018.04.006>
18. O. Samoilo, N. Shaburova, K. Pashkev, M. Samoduriva, and E. Trofimo, Al<sub>0.25</sub>CoCrFeNiV High Entropy Alloy Coating Deposited by Laser Cladding on Stainless Steel, *Materials*, 2022, **15**, p 7058. <https://doi.org/10.3390/ma15207058>
19. Y.Y. Chang and C.H. Chung, Tribological and Mechanical Properties of Multicomponent CrVTiNbZr(N) Coatings, *Coatings*, 2021, **11**, p 41. <https://doi.org/10.3390/coatings11010041>
20. E.G. Campari, A. Casagrande, E. Colombini, M.L. Gualtieri, and P. Veronesi, The Effect of Zr Addition on Melting Temperature Microstructure, Recrystallization and Mechanical Properties of a Cantor High Entropy Alloy, *Materials*, 2021, **14**, p 5994. <https://doi.org/10.3390/ma14205994>
21. J. Zhang, X. Xu, Y. Gao, G. Chen, W. Chen, and X. You, Effect of Zr Addition on Microstructure and Properties of Al-Mn-Si-Zn-Based Alloy, *Trans. Nonferrous Met. Soc. China*, 2014, **24**, p 3872–3878. [https://doi.org/10.1016/S1003-6326\(14\)63545-7](https://doi.org/10.1016/S1003-6326(14)63545-7)
22. J. Chen, P. Miu, Y. Liu, Y. Lu, X. Wang, Y. Peng, and J. Liu, Effect of Zr Content on Microstructure and Mechanical Properties of AlCoCr-FeNi High Entropy Alloy, *Mater. Des.*, 2016, **94**, p 39–44. <https://doi.org/10.1016/j.matdes.2016.01.033>
23. A. Amanov, Y.-S. Pyin, J.-H. Kim, and S. Sasaki, The Usability and Preliminary Effectiveness of Ultrasonic Nanocrystalline Surface Modification Technique on Surface Properties of Silicon Carbide, *Appl. Surf. Sci.*, 2014, **311**, p 448–460. <https://doi.org/10.1016/j.apsusc.2014.05.089>
24. L. Aihua, D. Jianxin, C. Haibing, C. Yangyang, and Z. Jun, Friction and Wear properties of TiNTiAlN, AlTiN and CrAlN PVD Nitride Coatings, *Int. J. Refract. Met. Hard Mater.*, 2012, **31**, p 82–88. <https://doi.org/10.1016/j.ijrmhm.2011.0>
25. P. Panjan, A. Drmovsek, P. Gselman, M. Cekada, and M. Panjan, Review of Growth Defects in Thin Films Prepared by PVD Techniques, *Coatings*, 2020, **10**, p 477. <https://doi.org/10.3390/coatings10050447>
26. P. Siemroth, M. Laux, H. Pursch, J. Sachtleben, M. Balden, V. Rohde, and R. Neu, Diameters and Velocities of Droplets Emitted from the Cu Cathode of a Vacuum Arc, *IEEE Trans. Plasma Sci.*, 2018, **47**, p 3470–3477. <https://doi.org/10.1109/TPS.2019.2912518>
27. S. Grigoriev, A. Vereschaka, F. Milovich, N. Sitnikov, N. Andreev, J. Bublikov, C. Sotova, and I. Sadov, Investigation of the Influence of Microdroplets on the Coatings Nanolayer Structure, *Coatings*, 2020, **10**, p 1204. <https://doi.org/10.3390/coatings10121204>
28. B. Murty, *High-Entropy Alloys*, Elsevier, Amsterdam, 2014
29. A. Patterson, The Scherrer Formula for x-ray Particle Size Determination, *Phys. Rev.*, 1939, **56**, p 978–982. <https://doi.org/10.1103/PhysRev.56.978>
30. N. Nussbaum, M.A.P. Yazdi, A. Michau, E. Monsifrot, F. Schuster, H. Maskrot, and A. Billard, Mechanical Properties and High Temperature Oxidation Resistance of (AlCrTiV)<sub>N</sub> Coatings Synthesized by Cathodic Arc Evaporation, *Surf. Coat. Technol.*, 2022, **434**, p 128228. <https://doi.org/10.1016/j.surfcoat.2022.128228>
31. L. Karlsson, A. Horlins, M.P. Johansson, L. Hultman, and G. Ramanath, The Influence of Thermal Annealing on Residual Stresses and Mechanical Properties of Arc-evaporated TiC<sub>x</sub>N<sub>1-x</sub> (x = 0, 0.15 and 0.45) thin films, *Acta Mater.*, 2002, **50**, p 5103–5114. [https://doi.org/10.1016/S1359-6454\(02\)00365-8](https://doi.org/10.1016/S1359-6454(02)00365-8)
32. K. Yalamanchili, F. Wang, I.C. Schramm, J.M. Andersson, M.P. Johansson Jöesaar, F. Tasnádi, F. Mücklich, N. Ghafoor, and M. Odén, Exploring the High Entropy Alloy Concept in (AlTiVNbCr)<sub>N</sub>, *Thin Solid Films*, 2017, **636**, p 346–352. <https://doi.org/10.1016/j.tsf.2017.06.029>
33. A. Kirmbauer, A. Kretschmer, C.M. Koller, T. Wojcik, V. Paneta, M. Hans, J.M. Schneider, P. Polcik, and P.H. Mayrhofer, Mechanical Properties and Thermal Stability of Reactively Sputtered Multi-principal-Metal Hf-Ta-Ti-V-Zr Nitrides, *Surf. Coat. Technol.*, 2020, **389**, p 125674. <https://doi.org/10.1016/j.surfcoat.2020.125674>
34. Q. Yang, L. Zhao, and P. Patnaik, Solid particle erosion resistant hard coatings for gas turbine engine applications. *Progress in Aircraft Icing and Aircraft Erosion Research*, Nova Science Publishers, Inc., 2017, p. 83–134
35. C. Feng, X. Huang, and Q. Yang, Mechanical Properties, Sliding Wear and Solid Particle Erosion Behaviours of Plasma Enhanced Magnetron Sputtering CrSiCN Coating Systems, *Wear*, 2014, **324–325**, p 27–35. <https://doi.org/10.1016/j.wear.2014.11.008>
36. G. Azar, C. Yelkarasi, and M. Urgan, The Role of Droplets on the Cavitation Erosion Damage of TiN Coatings, *Surf. Coat. Technol.*, 2017, **322**, p 211–217. <https://doi.org/10.1016/j.surfcoat.2017.05.050>
37. M. Tkadletz, C. Mitterer, B. Sartory, I. Letofsky-Papst, C. Czettl, and C. Michotte, The Effect of Droplets in Arc Evaporated TiAlTaN Hard Coatings on the Wear Behaviour, *Surf. Coat. Technol.*, 2014, **257**, p 95–101. <https://doi.org/10.1016/j.surfcoat.2014.01.010>
38. C.H. Lai, K.H. Cheng, S.J. Lin, and J.W. Yeh, Mechanical and Tribological Properties of Multi-element (AlCrTaTiZr)<sub>N</sub> Coatings, *Surf. Coat. Technol.*, 2008, **202**, p 3732–3738. <https://doi.org/10.1016/j.surfcoat.2008.01.014>
39. K.H. Cheng, C.H. Lai, S.J. Lin, and J.W. Yeh, Structural and Mechanical Properties of Multi-element (AlCrMoTaTiZr)<sub>N<sub>x</sub></sub> Coatings by Reactive Magnetron Sputtering, *Thin Solid Films*, 2011, **519**, p 3185–3190. <https://doi.org/10.1016/j.tsf.2010.11.034>
40. S.K. Bachani, C.J. Wang, B.S. Lou, L.C. Chang, and J.W. Lee, Fabrication of TiZrNbTaFeN High-Entropy Alloys Coatings by



- HiPIMS: Effect of Nitrogen Flow Rate on the Microstructural Development, Mechanical and Tribological Performance, Electrical Properties and Corrosion Characteristics, *J. Alloys Compd.*, 2021, **873**, p 159605. <https://doi.org/10.1016/j.jallcom.2021.159605>
41. A.D. Pogrebnjak, V.M. Beresnev, K.V. Smyrnova, Y.O. Kravchenko, P.V. Zukowski, and G.G. Bondarenko, The Influence of Nitrogen Pressure on the Fabrication of the Two-Phase Superhard Nanocomposite (TiZrNbAlYCr)N Coatings, *Mater. Lett.*, 2018, **211**, p 316–318. <https://doi.org/10.1016/j.matlet.2017.09.121>
42. A.D. Pogrebnjak, I.V. Yakushchenko, O.V. Bondar, V.M. Beresnev, K. Oyoshi, O.M. Ivasishin, H. Amekura, Y. Takeda, M. Opielak, and C. Kozak, Irradiation Resistance, Microstructure and Mechanical Properties of Nanostructured (TiZrHfVNbTa)N Coatings, *J. Alloys Compd.*, 2016, **679**, p 155–163. <https://doi.org/10.1016/j.jallcom.2016.04.064>
43. C. Wustefeld, D. Rafaja, V. Klemm, C. Michotte, and M. Kathrein, Effect of the Aluminium Content and the Bias Voltage on the Microstructure Formation in  $Ti_{1-x}Al_xN$  Protective Coatings Grown by Cathodic Arc Evaporation, *Surf. Coat. Technol.*, 2010, **205**, p 1345–1349. <https://doi.org/10.1016/j.surfcoat.2010.07.057>
44. A.E. Reiter, V.H. Derflinger, B. Hanselmann, T. Bachmann, and B. Sartory, Investigation of the Properties of  $Al_{1-x}Cr_xN$  Coatings Prepared by Cathodic Arc Evaporation, *Surf. Coat. Technol.*, 2005, **200**, p 2114–2122. <https://doi.org/10.1016/j.surfcoat.2005.01.043>
45. R. Boxman and S. Goldsmith, Macroparticle Contamination in Cathodic Arc Coatings: Generation, *Surf. Coat. Technol.*, 1992, **52**, p 39–50. [https://doi.org/10.1016/0257-8972\(92\)90369-L](https://doi.org/10.1016/0257-8972(92)90369-L)
46. M.H. Tsai and J.W. Yeh, High-Entropy Alloys: A Critical Review, *Mater. Res. Lett.*, 2014, **2**, p 107–123. <https://doi.org/10.1080/21663831.2014.912690>
47. M.H. Tsai, Physical Properties of High Entropy Alloys, *Entropy*, 2013 <https://doi.org/10.3390/e15125338>
48. S. Chen, W. Yan, Y. Zhao, Q. Li, L. Chen, X. Ouyang, Q. Hua, X. Wu, Y. Zhang, B. Liao, and X. Ouyang, Strong Amorphization of AlCrNiTiV High-Entropy Alloy Films Deposited by Cofilter Cathode Vacuum Arc Deposition, *Appl. Surf. Sci.*, 2022, **592**, p 153318. <https://doi.org/10.1016/j.apsusc.2022.153318>

**Publisher's Note** Springer Nature remains neutral with regard to jurisdictional claims in published maps and institutional affiliations.

Springer Nature or its licensor (e.g. a society or other partner) holds exclusive rights to this article under a publishing agreement with the author(s) or other rightsholder(s); author self-archiving of the accepted manuscript version of this article is solely governed by the terms of such publishing agreement and applicable law.